

pubs.acs.org/JPCC Article

Photoluminescence in Cerium-Doped Fluoride Borate Crystals

Talgat M. Inerbaev, Yulun Han, Tatyana B. Bekker,* and Dmitri S. Kilin*



Cite This: J. Phys. Chem. C 2023, 127, 9213-9224



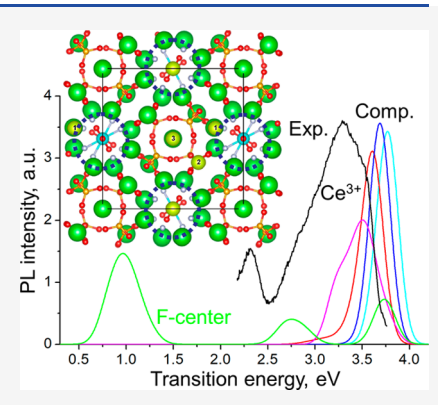
ACCESS I

Metrics & More

Article Recommendations

Supporting Information

ABSTRACT: Antizeolite fluoride borates LiBa₁₂(BO₃)₇F₄ (LBBF) doped by Ce³⁺ ions demonstrate photoluminescence (PL) and hold promise for use as phosphors in white light-emitting diodes. In this study, we present the results of modeling the electronic and optical properties of Ce-containing LBBF structures where doping atoms are located at different sites of the host lattice. We also consider the presence of F-centers, which exhibit trap states located within the band gap. We further investigate the nonadiabatic excited state electronic dynamics to elucidate electron-relaxation pathways. The nonadiabatic couplings (NACs) calculations provide transition probabilities facilitated by the nuclear movement. The relaxation rates of electrons and holes are calculated using Redfield's theory of the formalism of the reduced density matrix (RDM). The PL spectra are calculated using molecular dynamics (MD) sampling and time-integrated methods along the excited state trajectory based on NACs. Mechanisms of PL in LBBF:Ce³⁺ crystals are interpreted using both computational and experimental observations. This work illustrates the dependence of transition energies, intensities, and relaxation rates of Ce-containing



LBBF crystals on a selection of doping sites. In addition to analysis of emission band contributed by cerium, this work allows to identify and reproduce spectral lines hypothetically corresponding to the interband and intraband transitions in F-centers of borate crystals, available in the absence of a metal center.

1. INTRODUCTION

The study of borate systems is a research field developing at the intersection of crystal chemistry and materials science. Borates are promising compounds due to their chemical diversity and many areas of practical applications. ^{1–3} Phosphors based on these compounds are important for the dosimetry of ionizing radiation and personnel monitoring, and medical dosimetry, etc. ^{4,5}

Using borate crystals as a white light-emitting (WLED) diode matrix is a relatively new area of active development. WLEDs have many advantages compared to conventional light sources. Traditional light-emitting diodes (LEDs) emit monochromatic light, but WLEDs emit polychromatic light. The first method is the multi-LED chip approach, which mixes the three primary colors of light (red, green, and blue) and produces white light.⁶ The second method uses ultraviolet (UV) or violet LED chips and phosphors, which absorb UV or violet light and convert it into broadband white light. The now-obsolete Hg-based fluorescent lamp converted the deep UV light emitted by a Hg-vapor source ($\lambda = 254$ nm) into visible white light by means of a phosphor,8 which was proposed before the introduction of blue LEDs. The phosphor conversion method is the third and most successful approach, where a blue LED-chip-plus-phosphor combination with the phosphor emits green and red light. The phosphor partially absorbs the blue light from the LED chip, and the other blue light is transmitted through the phosphor. As a result, the blue light (from the LED chip) and green and red light (from the phosphor) form white light.⁹

The main components of WLEDs are chips and phosphors, which convert part of the chip's radiation by photoluminescence (PL). Researchers currently study phosphors based on host matrices of various compositions and lattice symmetries, functionalized with different activators. The activator is the luminescent center (small amounts of impurity ions in the system), and the matrix is the main part of the material. Impurities ions are introduced into the material to create levels of defects that play a crucial role in the material's luminescent properties. In recent years, rare-earth luminescent mixed inorganic materials have been an up-and-coming research topic due to the assembly of different cation or anion combinations, resulting in outstanding properties of such newly formed composite inorganic materials.

The most commonly used phosphors are yellow phosphors based on yttrium—aluminum garnet $(Y_3Al_5O_{12})$ activated with Ce^{3+} ions and highly efficient under blue excitation of chips based on the InGaN/GaN heterostructure. Some blue light is absorbed by the thin layer of $Y_3Al_5O_{12}$: Ce^{3+} phosphors and

Received: December 13, 2022 Revised: March 27, 2023 Published: May 9, 2023





converted to yellow light at a maximum wavelength of 550 nm. Blue and yellow combinations produce bright white light sources. The maximum emission bands between 525 and 585 nm can be changed by introducing a coactivator. The WLEDs with $\rm Y_3Al_5O_{12}:Ce^{3+}$ phosphors have a correlated color temperature of 5200 K and color rendering index (CRI, Ra) of 71. Al-16 One disadvantage of LEDs is the lack of high color white light. LED chips emitting near-ultraviolet radiation combined with red, green, and blue phosphors allow them to emit white light with a lower correlated color temperature and a higher CRI than $\rm Y_3Al_5O_{12}:Ce^{3+}$ phosphors.

Borate crystals were used as host matrices to produce red phosphors and red–green–blue (RGB) composite LEDs such as $ScCaOBO_3{:}Ce^{3^+}{,}Mn^{2^+}{,}^{20}$ $NaBaSc(BO_3)_2{:}Ce^{3^+}{,}Mn^{2^+}{,}^{21}$ $Ba_3Sc(BO_3)_3{:}Eu^{2^+}{,}^{22}$ $LaSc_3(BO_3)_4{:}Eu^{3^+}{,}^{23}$ and Li- $Ba_{12}(BO_3)_7F_4{:}Eu^{2^+}{,}^{24}$ To achieve white radiation one mixed radiation from several activators within one matrix such as $Ca_3Y(GaO)_3(BO_3)_4{:}Ce^{3^+}{,}Tb^{3^+}{,}Sm^{3^+}{,}^{25}$ and $Ca_3Gd-(AlO)_3(BO_3)_4{:}Ce^{3^+}{,}Tb^{3^+}{,}^{26}$

Compounds LiBa₁₂(BO₃)₇F₄ were previously described by Zhao and Li²⁷ and their structures were reinvestigated in ref 28. The nature of the variously colored LiBa₁₂(BO₃)₇F₄ crystals was discussed in ref 29. Luminescent properties of LiBa₁₂(BO₃)₇F₄ doped with Eu³⁺, Tb³⁺, and Ce³⁺ in different combinations were recently studied.³⁰ PL processes of coppercontaining borates were studied using *ab initio* calculation methods.³¹

First-principles treatment of basic properties of transparent host matrices activated by lanthanide ions needs spin-polarized (SP) and noncollinear spin (NCS) density functional theory (DFT) as a minimal level of theory to account for substantial number of unpaired spins³² and spin—orbit coupling (SOC).³³ First-principles treatment of photoluminescence for a broad range of solids can be performed on the basis of first-principles molecular dynamics (MD). A random thermal motion of ions in a model represents thermal broadening of spectral lines and serves as a reason for nonradiative transitions.³⁴ This methodology was earlier tested in application to NaYF₄ matrix activated by Ce³⁺ ions^{35,36} and Pr³⁺ ions.^{33,35,36}

In calculations, we relied on well-known experimental data that cerium ions enter the borate matrix in the +3 state. PL emission spectra in the range of about 320-450 nm accounted for 4f-5d electron transition of Ce³⁺ were reported in several works, which considered the inclusion of trivalent cerium ions in the lattice of the studied borate³⁰ and other host lattices such as $Ca_xSr_{1-x}BP_5O_{20}$: Ce^{3+37} and $Ba_6AlP_5O_{20}$: Ce^{3+38} and α - $Sr_2P_2O_7$: Ce^{3+} phosphors³⁹ and Li₃YCl₆: Ce^{3+} ,⁴⁰ Lu₂Si₂O₇: Ce^{3+} ,⁴¹ and BaBrI: Ce^{3+} scintillators.⁴² Three types of electronic transitions can take place involving trivalent lanthanide ions. 43 (i) Charge transfer transition. 44 Both ligandto-metal and metal-to-ligand transitions are allowed by Laporte's selection rule. They appear in the UV range λ < ~250 nm, except for ions which may be easily either reduced to their +2 state (Sm, Eu, Tm, Yb), or oxidized to their +4 state (Ce, Pr, Tb). (ii) 4f-5d transitions. 45 Ce3+ doped compounds generally show 5d-4f emission in the near UV, but in case of high crystal field splitting, such as in garnets, visible emission is sometimes observed. The crystal field splitting of the 5d levels of Ce³⁺ ions in different coordination has been extensively investigated. (iii) f-f transitions. 46 The sharp f-f transitions involve a rearrangement of the electrons in the 4f subshell and are therefore polarity forbidden, which explains their faint intensities. For Ce3+ with only one 4f

electron the situation is relatively simple. As there are no 4f electrons in the $4f^{n-1}$ 5d excited state, the parameters for 4f-4f and 4f-5d interactions do not play a role. The energy level structure arises from the splitting of the 5d state determined by crystal field parameters, covalency effects and SOC.

A newly discovered class of LiBa₁₂(BO₃)₇F₄ borates (referred further as LBBF) has contributed to the diversity of borates crystal chemistry. The LBBF crystal belongs to the group of "antizeolite" borates with a $[Ba_{12}(BO_3)_6]^{6+}$ cation "framework" (ideal symmetry I4/mcm) and (pseudo)-tetragonal channels along c axis formed by altering cubes and anticubes.²⁸ Cubic cages are occupied by $[LiF_4]^{3-}$ clusters, whereas anticubes are occupied by $(BO_3)^{3-}$ groups (Figure 1a,b). Thus, the structural formula of LBBF can be represented as $Ba_{12}(BO_3)_6[BO_3][LiF_4]$.

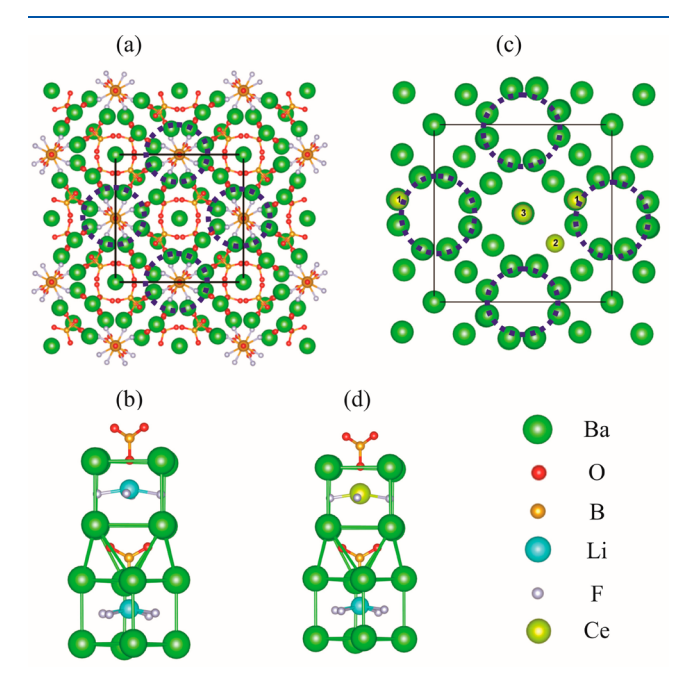


Figure 1. (a) Crystal structure of Ba₁₂(BO₃)₆[BO₃][LiF₄] with channels highlighted in dashed circles. (b) Channels in Ba₁₂(BO₃)₆[BO₃][LiF₄] with [LiF₄]³⁻ in cubic and [BO₃]³⁻ in anticubic cages. (c) Ce@Ba structure, where Ce ions replace Ba ions at enumerated positions as described in the text. Only the Ba–Ce framework is shown, and all anions are hidden to read the figure easily. (d) Channels in Ba₁₂(BO₃)₆[BO₃][LiF₄] with [LiF₄]³⁻ where one Li ion substituted was with Ce (structure Ce@Li). See text for a detailed description of F-center creation.

In the present study, we first carry out DFT calculations on electronic and optical properties of Ce-containing LBBF structures where doping atoms are located at different sites of the host lattice. Previous studies have shown that the presence of defects such as F-centers is critical in describing the optical absorption spectra of antizeolite borates. ²⁹ For this reason, in addition to the effect of doping with Ce ions, we study the contribution of F-centers. We then investigate the nonadiabatic excited state electronic dynamics in borate crystals to elucidate electron-relaxation pathways. The onthe-fly nonadiabatic couplings (NACs) calculations provide transition probabilities facilitated by nuclear movements. The relaxation rates of electrons and holes are calculated using Redfield's theory with the formalism of the reduced density matrix (RDM). ^{49–52} Computational PL spectra are calculated

using MD sampling methods³⁴ and time-integrated methods⁵³ along the excited state trajectory based on NACs. Mechanisms of PL in LBBF:Ce³⁺ crystals are interpreted using both computational and experimental observations.

2. METHODS

2.1. Theoretical Approaches. Computational characterization of materials' properties is achieved in five directions: (i) ground state electronic structures, (ii) linear optical absorption, (iii) thermal motion of nuclei, (iv) nonradiative transitions, and (v) photoluminescence.

2.1.i. Ground State Electronic Structures. Ce3+ ions have one unpaired 4f electron. Accurate analysis of the open-shell system requires the use of SP or NCS DFT calculations. An important issue facing theoretical modeling of the considered materials is the necessity to include SOC due to the heavy Ba and Ce elements. NCS DFT has been used to calculate the effects of SOC upon the ground-state electronic structures of the modeled systems.⁵⁴ In the SP basis, spin is a good quantum number and is conserved for dipole allowed optical transitions. In contrast, when working in the spinor Kohn-Sham orbitals (SKSO) basis, the total angular momentum J = L+S is the conserved quantity and allows for changes in spin during excited state dynamics, such as the dipole-forbidden tripletsinglet optical transition or nonradiative spin-flip relaxation. However, for NCS calculations, spin is not a good quantum number, and therefore, there are no spin up and spin down orbitals. Instead, one finds energies of spinor states, which are composed of both up and down components.

Within the NCS DFT framework, relativistic effects can be incorporated using second-order scalar relativistic corrections and SOC

$$\hat{H}^{rel} = \hat{H}^{scalar} + \hat{H}^{SOC}; \, \hat{H}^{SOC} = \frac{\hbar}{4m^2c^2} \frac{1}{r} \frac{\partial v_{sphere}^{KS}}{\partial r} (\mathbf{L} \cdot \mathbf{S})$$
(1)

where L is the angular momentum operator and S is composed of Pauli spin matrices. The relativistic Hamiltonian from eq 1 is composed of two terms: \hat{H}^{scalar} is the scalar relativistic term and \hat{H}^{SOC} is the SOC term. \hat{H}^{scalar} term describes relativistic kinetic energy corrections and \hat{H}^{SOC} describes energy shifts of spin occupations. The Kohn–Sham equations for components of a spinor orbital read

$$\sum_{\sigma'=\alpha,\beta} \left(-\delta_{\sigma\sigma'} \nabla^2 + v_{\sigma\sigma'}^{\text{eff}}(\mathbf{r}) \right) \psi_{i\sigma'}(\mathbf{r}) = \varepsilon_i^{NCS} \psi_{i\sigma}(\mathbf{r})$$
(2)

Note that for SP DFT nondiagonal components $v_{\alpha\beta}^{\rm eff}=0$, while for the NCS approach $v_{\alpha\beta}^{\rm eff}\neq0$. The NCS DFT procedure provides components of spinor orbitals representing two-component vectors

$$\psi_i^{KS}(\mathbf{r}) = \begin{pmatrix} \psi_{i\alpha}(\mathbf{r}) \\ \psi_{i\beta}(\mathbf{r}) \end{pmatrix}$$
(3a)

In NCS DFT SKSO electron density has a matrix form

$$\rho^{NCS}(\mathbf{r}) = \begin{pmatrix} \rho_{\alpha\alpha} & \rho_{\alpha\beta} \\ \rho_{\beta\alpha} & \rho_{\beta\beta} \end{pmatrix} \tag{3b}$$

Components within the density matrix are found from

$$\rho_{\sigma\sigma'} = \sum_{i} f_{i}^{NCS} \psi_{i\sigma}^{NCS}(\mathbf{r}) \psi_{i\sigma'}^{NCS}(\mathbf{r})$$
(3c)

where f_i^{NCS} is the occupation number of the *i*th SKSO and takes values between 0 and 1. Spin-polarized orbitals of the same index with opposite spin projections experience mixing due to spin-orbit interaction. This methodology has been detailed in a previous work.³⁶

2.1.ii. Linear Optical Absorption. The transition dipole moment in NCS calculations, \mathbf{D}_{ij} , is calculated within the independent orbital approximation (IOA)^{55–57} between each set of two specified orbital pairs, i and j, according to

$$\mathbf{D}_{ij} = e \int d\mathbf{r} \left\{ \psi_{i\alpha}^*(\mathbf{r}, \mathbf{R}_{\mathbf{I}}(t)) \psi_{i\beta}^*(\mathbf{r}, \mathbf{R}_{\mathbf{I}}(t)) \right\} \mathbf{r} \begin{cases} \psi_{j\alpha}(\mathbf{r}, \mathbf{R}_{\mathbf{I}}(t)) \\ \psi_{j\beta}(\mathbf{r}, \mathbf{R}_{\mathbf{I}}(t)) \end{cases}$$
(4)

The transition dipole moment is then used to calculate the oscillator strength, f_{ij} , for the corresponding transition using $f_{ij} = \frac{4\pi m_e e_{ij}}{3\hbar^2 e^2} |D_{ij}|^2$, where $\varepsilon_{ij} = \varepsilon_i - \varepsilon_j$ is the transition energy between i^{th} and j^{th} spinor electronic levels; \hbar , e, and m_e are the Planck constant, elementary charge, and mass of the electron, respectively. Note that in the NCS approach, there is a summation over spin indices in a procedure to compute matrix elements. The linear optical absorption spectrum as a function of the incident radiation energy ε is calculated using the delta function to provide thermal broadening,

$$\alpha(\varepsilon) = \sum_{ij} f_{ij} \delta(\varepsilon - \varepsilon_{ij}) \tag{5}$$

2.1.iii. Thermal Motion of Nuclei. Modeling atomic motion is accomplished by heating and adiabatic MD simulations. The atomistic system interacts with a thermostat of a chosen temperature with rescaled momenta, $\mathbf{P_{I}}$, at each time step $\sum_{I=1}^{N_{lons}} \frac{\mathbf{P_{I}^{2}}}{2M_{I}} = \frac{3}{2}N_{lons}k_{B}T$. Upon reaching thermal stability, the nuclear momenta are used as input to calculate an MD trajectory of the adiabatic ground state as a function of time by Newton's equation of motion. The atomic coordinates are collected at each time step of the MD trajectory, allowing for a single-point electronic structure analysis.

2.1.iv. Nonradiative Transitions. The time evolution of the electronic degrees of freedom is calculated by solving the equation of motion,

$$\frac{\mathrm{d}\rho_{ij}}{\mathrm{d}t} = -\frac{i}{\hbar} \sum_{k} \left(F_{ik} \rho_{kj} - \rho_{ik} F_{kj} \right) + \left(\frac{\mathrm{d}\rho_{ij}}{\mathrm{d}t} \right)_{diss} \tag{6}$$

Here, the Fock matrix corresponds to the adiabatic contribution and $\left(\frac{\mathrm{d}\rho_{ij}}{\mathrm{d}t}\right)_{diss}$ represents the electronic dissipative

transitions that are facilitated by the motion of ions and computed along the MD trajectory. NACs can be computed according to the on-the-fly procedure along the nuclear trajectory as a measure of violation of spinor orbital orthogonality in eq 3, due to nuclear motion.

$$V_{ij}^{NA}(t) = -\frac{i\hbar}{2\Delta t} \int d\mathbf{r} \left\{ \psi_{i\alpha}^*(\mathbf{r}, \mathbf{R}_{\mathbf{I}}(t + \Delta t)) \right\} \begin{cases} \psi_{j\alpha}(\mathbf{r}, \mathbf{R}_{\mathbf{I}}(t)) \\ \psi_{j\beta}(\mathbf{r}, \mathbf{R}_{\mathbf{I}}(t)) \end{cases}$$

$$(7a)$$

Equation 7a does make a summation of the spin projections and, as a result, coupling $V_{ij}^{\rm NA}$ (t) does not include the spin index. The autocorrelation function $M_{ijkl}(\tau) = \int_0^\infty V_{ij}(t+\tau) V_{kl}(t) \, dt$ and the following Fourier transform provide elements of Redfield tensor (\hat{R}) , which controls the dissipative dynamics of the density matrix

$$\left(\frac{\mathrm{d}\rho_{ij}}{\mathrm{d}t}\right)_{diss} = \sum_{kl} R_{ijkl}\rho_{kl} \tag{7b}$$

The solution of eqs 6-7a and 7b provides several observables including the charge density distribution, rate of energy distribution, and rate of charge transfer. The nonequilibrium distribution of charge as a function of time and energy reads

$$n^{(a,b)}(\varepsilon,t) = \sum_{i} \rho_{ii}^{(a,b)} \delta(\varepsilon - \varepsilon_{i})$$
(8)

where (a,b) is corresponding to the initial photoexcitation from state a to b. The change in population from the equilibrium distribution is

$$\Delta n^{(a,b)}(\varepsilon,t) = n^{(a,b)}(\varepsilon,t) - n^{eq}(\varepsilon,t) \tag{9}$$

where $\Delta n > 0$ in the equation describes the population gain and $\Delta n < 0$ the population loss.

2.1.v. Photoluminescence. One calculates the time-resolved and time-integrated PL as follows.

$$E^{PL}(\varepsilon, t) = \sum_{ij} f_{ij} \delta(\varepsilon - \varepsilon_{ij}) (\rho_{jj}(t) - \rho_{ii}(t))$$
(10)

$$E^{PL}(\varepsilon) = \int_0^T E^{PL}(\varepsilon, t) dt$$
 (11)

where T stands for the duration of the time-integration interval. An emission event between a pair of orbitals may occur if inverse population conditions are satisfied where $\rho_{jj} > \rho_{ii}$, $\varepsilon_j > \varepsilon_i$.

2.2. Computation Details. The electronic structures, which account for Coulomb, correlation, and exchange electron-electron interactions and interactions of electrons with ions, were computed with DFT by self-consistent solving of the Kohn-Sham equations as implemented in the Vienna ab initio simulation package (VASP). 58,59 The Perdew-Burke-Ernzerhof (PBE)60 exchange-correlation functional under the generalized gradient approximation (GGA)⁶¹ and the hybrid functional Heyd-Scuseria-Ernzerhof (HSE06)62 were used. The mixing parameter defining the amount of the exact Hartree-Fock exchange was chosen to be 0.25. This choice described well the bandgap of the fluoride borate crystals.^{29,63} The on-site Coulomb correlation of f-electrons was taken into account employing Hubbard corrections in the Dudarev parametrization with a *U-J* value of 5.5 eV for cerium. ^{64,65} Calculations were done using the projector augmented-wave (PAW)⁶⁶ formalism, which was developed using the concept of pseudopotentials in the plane-wave basis.

Ground state electronic structure calculations performed using HSE06 functional provided more accurate band gap

energies than PBE. However, because the same trends were observed, we preferred PBE to HSE06 considering its low computational cost. For adiabatic MD calculations, geometry-optimized models were heated to 77 or 300 K by a Nose—Hoover thermostat with repeated velocity rescaling. Then, 1 ps microcanonical trajectories were generated using the Verlet algorithm⁶⁷ with a time step of 1 fs. Atomic structures were visualized in the VESTA package.⁶⁸ We used the VASPKIT code to postprocess the calculated data from VASP.⁶⁹

For the numerical study, the Ba₁₂(BO₃)₆[BO₃][LiF₄] unit cell of $P4_2bc$ symmetry containing four formula units was taken as the initial structure.²⁸ We considered several structural motifs to incorporate Ce3+ into LBBF and to account for Fcenters. (i) One Ce atom replaced one Ba atom in the framework of the antizeolite lattice. The Ba sublattice consisted of seven nonequivalent symmetry atoms, five at 8c sites and two at 4a sites in Wyckoff notation. The five Ba atoms located at 8c sites form lattice channels. The difference from the remaining type of atoms was that these atoms were closer to the complexes enclosed in the lattice cavities. Thus, we considered the following replacements of Ba atoms with Ce atoms. Ce1@Ba-replacing the Ba atom at position 8c, which forms a channel in the borate structure; Ce2@Ba-replacing the Ba atom at another position 8c, located between the channels; Ce3@Ba-replacing the Ba atom at the 4a site as shown in Figure 1c. In each case, one electron was removed to keep the cerium ion in the +3 oxidation state. (ii) One Ce atom replaced one Li atom in the cubic cage of the antizeolite lattice, labeled as Ce@Li (see Figure 1). Two electrons were then removed to keep the cerium ion in the +3 oxidation state. (iii) To consider the influence of F-centers, we employed the simplest case of the LBBF structure, in which one fluorine atom was removed. In this case, PL spectra were calculated using a spin-polarized approach, as in the study of Cu-doped

Note that we consider the contributions of the Ce³⁺ ions and F-centers independently, which corresponds to a low concentration of these defects. This should lead to a low probability of finding these defects at a close distance from each other. In calculations, when Ce³⁺ ions replace Ba²⁺ or Li⁺ ions, one electron or two electrons must be removed to maintain the oxidation state of cerium at +3. When one creates a center of charge for the F-center, namely the removal of one fluorine atom, the system remains charge neutral, and one excess electron is localized in the position of fluorine vacancy.

2.3. Experimental Details. Crystal Growth. We used BaCO₃, BaF₂, Li₂CO₃, H₃BO₃, and oxides of cerium of high purity grade as starting reagents. The batch (40 g) was melted in a platinum crucible (40 mm in diameter) at a heating rate of 25 °C/h for crystallization on a platinum loop to grow crystals. The liquidus temperature was about 760 °C. A platinum rod with the loop was placed in the central part of the melt surface at the liquidus temperature to induce crystallization. From the moment of detection of the first microcrystals, the solution was cooled at a rate of 2 °C per day to increase crystal size. The average duration of the growth experiment was about 10 days. Then the platinum loop with the grown crystals was extracted from the melt and cooled to room temperature at a rate of 15 °C/h. The weight of grown crystals was about 7 g. Note measurements of the concentration of cerium in doped crystals were difficult. The doping concentration of cerium was likely to be several hundredths of one percent, as suggested by the

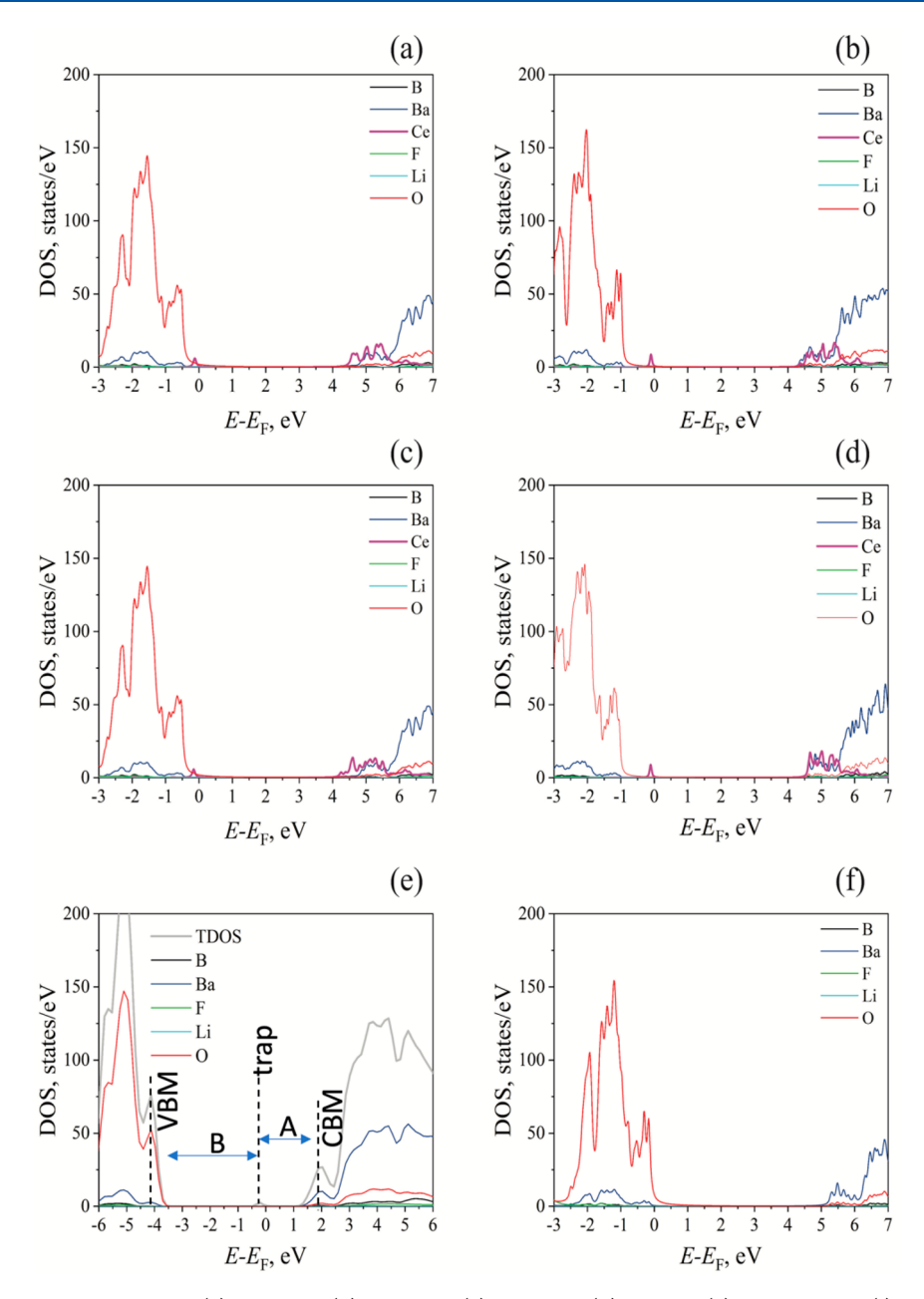


Figure 2. HSE06-SOC calculated DOS for (a) Ce1@Ba, (b) Ce2@Ba, (c) Ce3@Ba, (d) Ce@Li, (e) F-center, and (f) LBBF structures. Note an occupied trap state feature near the Fermi energy at the panel e. The interband transition "A" between the trap to the CBM is available for both linear absorption and emission at transition energy near 2 eV. The intraband transition "B" between VBM and the trap is not available for linear absorption, since both bands are occupied in the ground state. However, in the excited state, the population inversion condition may enable the transition "B". This radiative transition would be available for excited states featuring nonrecombined hole occupying VBM, prior to cascading to the trap via nonradiative channel. The transition "B" would occur at transition energy near 4 eV or lower, due to nuclear reorganization and thermal broadening.

doping concentration of other lanthanide ions in borate crystals grown using similar procedures.³⁰

Optical Spectroscopy. PL spectra of Ce-doped Ba₁₂(BO₃)₆[BO₃][LiF₄], i.e., LBBF:Ce³⁺ crystals, were recorded with a Horiba JobinYvon-Fluorolog 3 spectrofluorometer equipped with 450 W ozone-free Xe-lamp, cooled PC177CE010 photon detection module with a PMT R2658, and double grating excitation and emission monochromators. Standard correction curves were used to correct excitation and emission spectra for source intensity and emission spectral response. Optistat DN was used to investigate the temperature

dependencies of luminescence properties in the range 77-300 K.

Transmission spectra were measured using UV-vis-NIR spectrometer UV-3101 PC, Shimadzu. The thickness of the polished plate made from the crystal and used for measurements was about 1.2 mm.

3. RESULTS AND DISCUSSION

Figure 2 shows the HSE06 functional electronic density of states (DOS) calculated for the Ce-containing LBBF models, F-center, and undoped LBBF structures. A characteristic feature of the electronic structure of all Ce containing models

is that near the top of the valence band, occupied levels correspond to Ce-4f states. The electronic structures demonstrate a decrease in the energy of conduction band minimum (CBM) in the interval from 5.3 eV for LBBF to 4.2–4.5 eV, depending on the lattice site at which the Ce³⁺ ion is located (Figure 2a–d). This feature will be discussed in more detail when considering optical absorption in these systems. The F-center structure is characterized by the appearance of an electronic level in the band gap due to the presence in the system of an electron that is not bound to any atom and is located in the interatomic space of the lattice (Figure 3). This

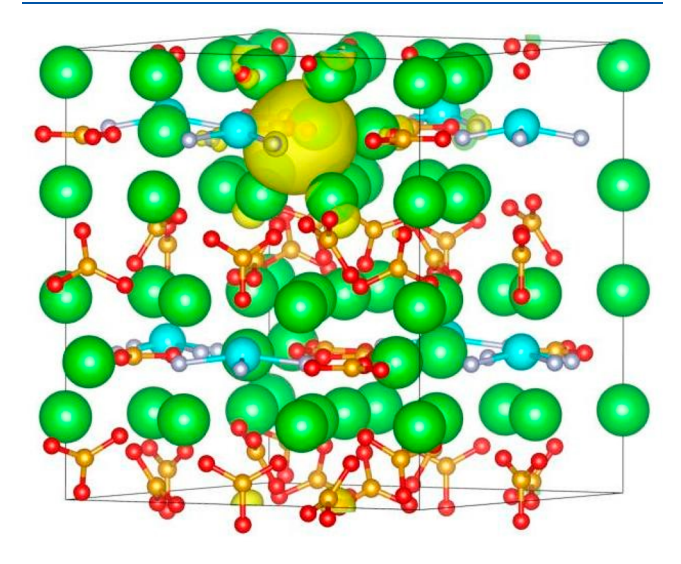


Figure 3. Partial charge density of the electronic state corresponding to the F-center model. Yellow clouds represent charge density isocontours. Atom coloring is the same as it is in Figure 1. This orbital corresponds to the occupied trap state feature near the Fermi energy in Figure 2e.

electronic state is located within the band gap of approximately 1.3 eV below the bottom of the conduction band (Figure 2e). This state specific to the F-center is labeled as the "trap" state. The interband transition "A" between the trap to the CBM is available for both linear absorption and emission at transition energy near 2 eV. The intraband transition "B" between the valence band maximum (VBM) and the trap is not available for linear absorption, since both bands are occupied in the ground state. However, in the excited state, the population inversion condition may enable the transition "B". This radiative transition would be available for excited states featuring nonrecombined holes occupying VBM, prior to cascading to the trap via nonradiative channel. The transition "B" would occur at transition energy near 4 eV or lower, due to nuclear reorganization and thermal broadening. The presence of defects does not affect the electronic states of the O-2p and Ba-5d states, which form states near the top of the valence band and the bottom of the conduction band in LBBF, respectively (Figure 2f).

It follows from the DOS values presented in Figure 2a–d that the optical properties of Ce-doped borates are determined by 5d–4f transitions on Ce³⁺ ions. Since Figure 2 shows data for the total DOS on Ce³⁺, it is necessary to consider the electronic structures of these ions in more detail. For this purpose, Figure 4 presents projected DOS (PDOS) on Ce³⁺ ions. It can be seen from the presented data that it is typical for unoccupied states that 5f states contribute more to DOS. The

densities of 5d states that are important for optical transitions can have a small value and be relatively uniformly spread starting from energies of 4.3–4.5 eV and higher in the cases of Ce1@Ba and Ce2@Ba structures, reaching maximum values at a point of 5.5 eV and higher (Figure 4a,b). For the Ce3@Ba and Ce@Li structures, the PDOS value for 5d states has a similar split peak (Figure 4c,d). In this case, for Ce3@Ba and Ce@Li, these peaks are located in the energy range of 4–4.5 eV and 4.5–5 eV, respectively. These features in the electronic structures of Ce³+ ions are due to their different local environments in the crystal.

Differences in the electronic structures of Ce³⁺ ions during their incorporation into the borate lattice also cause differences in the optical properties of the structures. Figure 5 shows the optical absorption spectra of the Ce-containing borates considered in this work compared to the experiment. According to experimental data, the absorption of LBBF:Ce³⁺ ranging from 1.5 to 3.0 eV is weak but then rapidly increases and reaches a plateau at energies from 4.2 to 5.2 eV, after which it becomes completely opaque. A line corresponding to the F-center demonstrates absorption at the low transition energy corresponding to the interband feature "A" in the DOS.

In the case of the Ce@Li structure, calculations predict that it should be transparent up to an energy of 4.8 eV. Then, up to an energy value of 5.6 eV, this compound should be practically transparent. A much better agreement with the experiment is demonstrated by Ce1@Ba and Ce2@Ba structures, in which Ce³+ ions occupy 8c lattice sites. The optical absorption spectrum for the Ce3@Ba structure is an intermediate between the case of Ce@Li and Ce1@Ba and Ce2@Ba structures. Here, it is necessary to consider that of all Ce@Ba configurations, the Ce2@Ba structure is the most energetically favorable (Supporting Information). In contrast, the Ce1@Ba and Ce3@Ba structures have a relative energy of 0.218 and 0.646 eV, respectively. Based on these data, the structures Ce1@Ba and Ce2@Ba of the considered variants are most likely to be realized in the experiment.

Figure 6 shows the excited-state dynamics of electron—hole pairs for the F-center, Ce2@Ba, and Ce@Li models. The results are obtained by processing NACs from adiabatic MD trajectories using SP DFT for the F-center and NCS DFT for the other models. The blue and orange colors represent the gain of population for holes and electrons, respectively, as introduced in eq 9. The green color represents no change, i.e., ground-state charge density. The solid and dashed lines indicate the energy expectation values for holes and electrons in the excited states, respectively.

Each panel displays the distribution of electronic populations as a function of energy and time. At the initial time of each panel, there is an instantaneous excitation, which excites electrons to the LU+y (yth orbital above lowest unoccupied molecular orbital) in the conduction band and introduces holes to the HO-x (xth orbital below highest occupied molecular orbital) orbital in the valence band. These excitations HO- $x \rightarrow$ LU+y correspond to optical transitions with high oscillator strengths. After the excitation, the excited electrons relax to the LU and the holes to the HO through the nonradiative process of vibrational relaxation. Note here the electron—hole pairs remain at the frontier orbitals for a certain time prior to relaxing back to the ground electronic state.

The left panels of Figure 6 illustrate the dynamics at 77 K, while the right panels show the dynamics at 300 K. For each row, the same initial condition is used to compute dynamics at

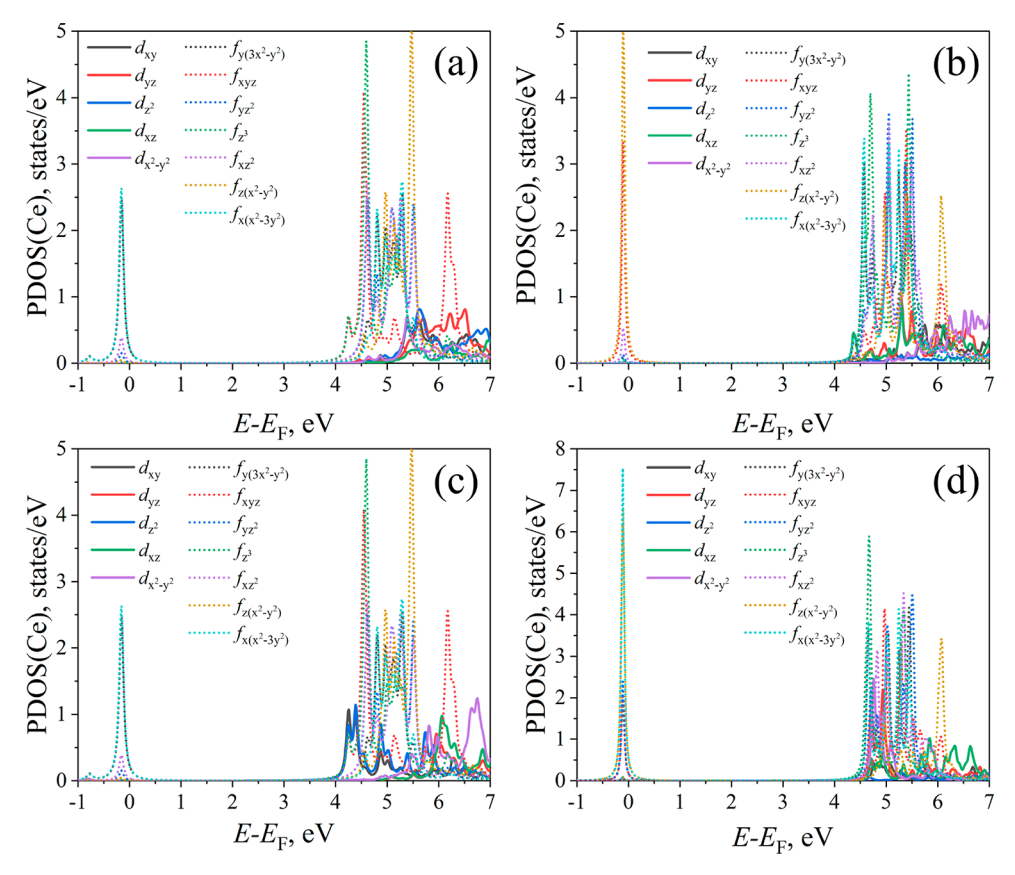


Figure 4. HSE06-SOC calculated PDOS on Ce³⁺ ions in (a) Ce1@Ba, (b) Ce2@Ba, (c) Ce3@Ba, and (d) Ce@Li structures. Solid lines correspond to Ce-5d electronic states and dotted lines to Ce-4f states.

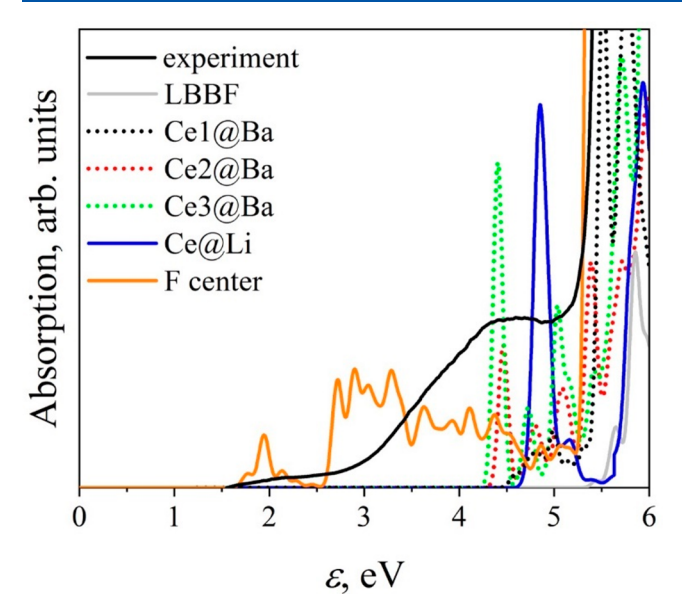


Figure 5. Absorption spectra of LBBF, Ce@Ba, Ce@Li, and F-center structures calculated with HSE06-SOC compared with experiment. The orange line corresponding to the F-center has several low-energy transitions, interpreted as the "A" transition from the trap to the CBM (LU) and a progression of subsequent transitions from the same group "trap" \rightarrow LU+1, "trap" \rightarrow LU+2 etc.

different temperatures. Comparing the dynamics at different temperatures, one finds similar relaxation patterns but noticeably different relaxation rates. Electrons and holes at the room temperature, in most cases, show much larger relaxation rates than that at 77 K. This is due to larger values of Redfield tensor elements from NACs calculations at higher temperatures, which describe state-to-state population transfer rates (see Supporting Information). The temperature dependence of nonradiative relaxation rates is due to resonance coupling between lattice vibrations and sublevels among electronic states.

Comparing the dynamics for various models, one finds the spin up component of F-center shows different relaxation patterns. There is a trap state between CBM and VBM for the spin up component of F-center, which is not observed for other models. The subgap between the trap state (HO) and VBM (HO-1) is about 3.7 eV, which requires multi-phonon mechanism of relaxation and thus greatly slows down the relaxation of holes. Due to the presence of long-lived trap state, one expects an intraband transition HO-1 \rightarrow HO (labeled as "B"), which contributes to the PL of F-center in addition to Kasha emission LU → HO (labeled as "A"). Among all models, the largest relaxation rates of electrons are observed for Ce@Li, whereas the largest relaxation rates of holes are observed for the spin down component of F-center. The relaxation rates of electrons and holes are mainly affected by orbital overlap and subgaps between electronic states. Table 1 summarizes the nonradiative relaxation rates corresponding to Figure 6.

We have studied the nonradiative transitions of electron-hole pairs for various models. Here, we focus on radiative transitions that is competing with nonradiative transitions. Figure 7 shows the time-integrated PL spectra computed along the excited-state dynamics trajectories for the F-center, Ce2@Ba, and Ce@Li models. The initial excitation conditions are

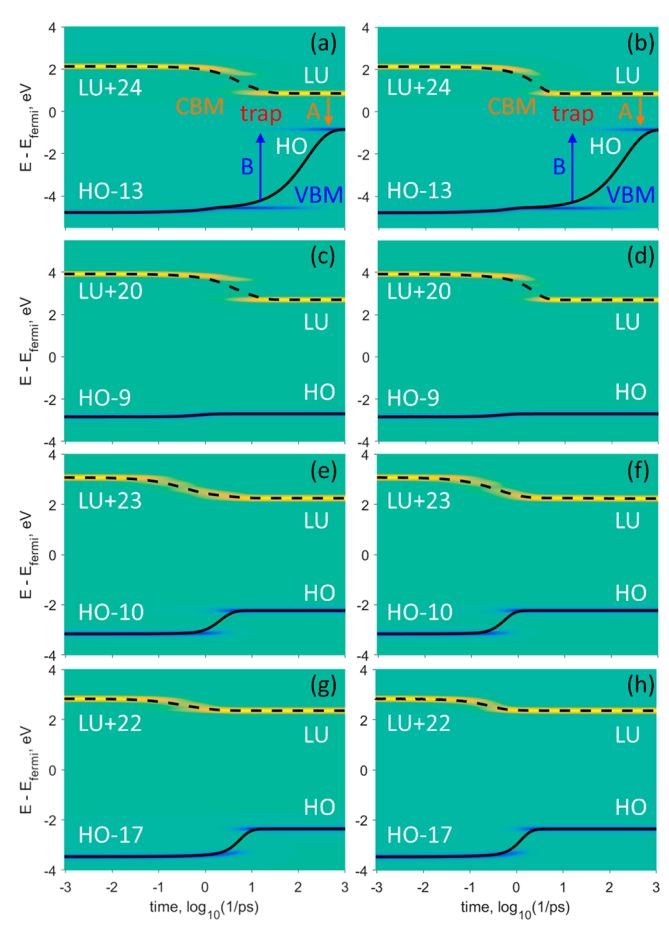


Figure 6. Charge carrier dynamics for (a, b) F-center spin α , (c, d) F-center spin β , (e, f) Ce2@Ba, and (g, h) Ce@Li. The left panels correspond to the dynamics at 77 K, while the right panels correspond to the dynamics at 300 K. The results are obtained by processing NACs from adiabatic molecular dynamics trajectories using SP DFT for the F-center and NCS DFT for the other models. The blue and yellow colors represent the gain of population for holes and electrons, respectively. The green color represents no change, i.e., ground-state charge density. The solid and dashed lines indicate the energy expectation values for holes and electrons in the excited states, respectively. There are several features labeled in panels a and b of F-center. Feature "A" represents Kasha emission LU \rightarrow HO, whereas feature "B" represents an intraband transition HO-1 \rightarrow HO.

the same as in Figure 6. There are two general observations: the spectra at 77 K are similar to the ones at 300 K and Kasha emission features LU \rightarrow HO dominate over other optical transitions. This is because the time the hot carriers take to reaching frontier orbitals is much shorter than the recombination time and the duration of the time-integration interval.

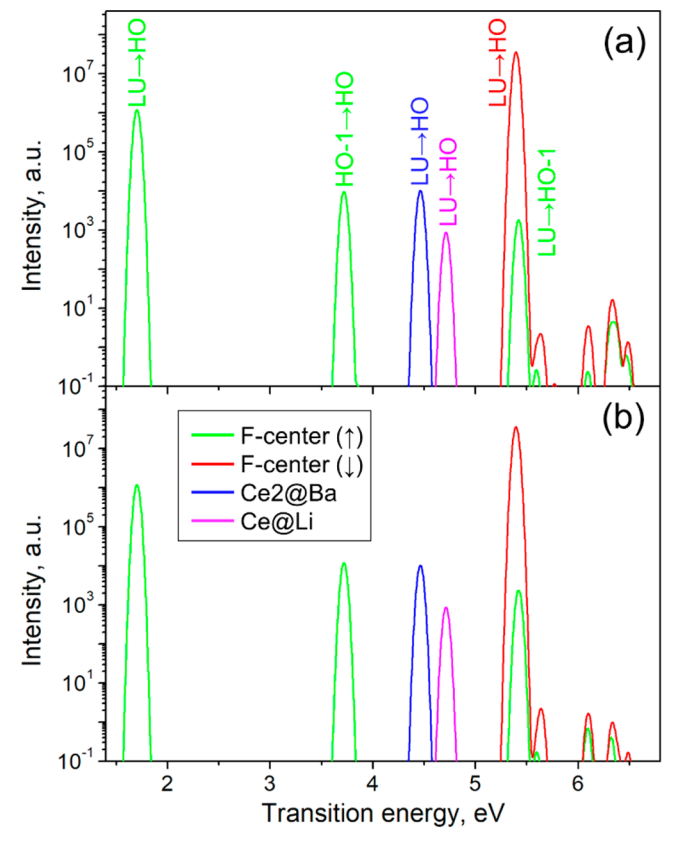


Figure 7. Time-integrated PL spectra computed along the excited-state dynamics trajectories for F-center, Ce2@Ba, and Ce@Li models. The results are obtained by processing NACs from adiabatic molecular dynamics trajectories using SP DFT for F-center and NCS DFT for the other models. The initial excitation conditions are the same as in Figure 6. Spectra from panel a correspond to dynamics at 77 K, while spectra in panel b correspond to dynamics at 300 K.

For the spin up component of F-center, features at 3.7 and 5.4 eV are also strong. The former corresponds to the intraband transition $HO-1 \rightarrow HO$, whereas the latter corresponds to the interband transition $LU \rightarrow HO-1$. These features are due to the presence of the long-lived trap state, as discussed in Figure 6. For the spin down component of F-center, Ce2@Ba, and Ce@Li models, intensities of non-Kasha transitions are several orders of magnitude weaker than the Kasha emission.

The PL spectra from excited-state trajectories in Figure 7 allow us to identify the most probable transitions. However, this method generates PL features with narrow line widths as a result of using averaged transition energies. To find a better agreement with experimental PL spectra, one should take into account the effect of thermal broadening. Such a method

Table 1. Nonradiative Relaxation Rates for Hot Electrons and Holes Following the Initial Photoexcitaions

model	initial excitation	transition energy, eV	oscillator strength	temperature, K	$k_{\rm e}$, ps ⁻¹	$k_{\rm h}$, ps ⁻¹
F-center (†)	$HO-13 \rightarrow LU+24$	6.9079	0.6933	77	0.1384	0.0069
				300	0.4792	0.0056
F-center (\downarrow)	$HO-9 \rightarrow LU+20$	6.7610	0.6748	77	0.1729	1.3984
				300	0.5632	2.5146
Ce2@Ba	$HO-10 \rightarrow LU+23$	6.2291	0.0128	77	0.3391	0.4731
				300	0.6265	2.0056
Ce@Li	$HO-17 \rightarrow LU+22$	6.2921	0.0095	77	1.7397	0.1939
				300	3.1246	0.8499

(molecular dynamics photoluminescence or MDPL) has been reported by a few of us.^{34,70} Figure 8 shows comparison

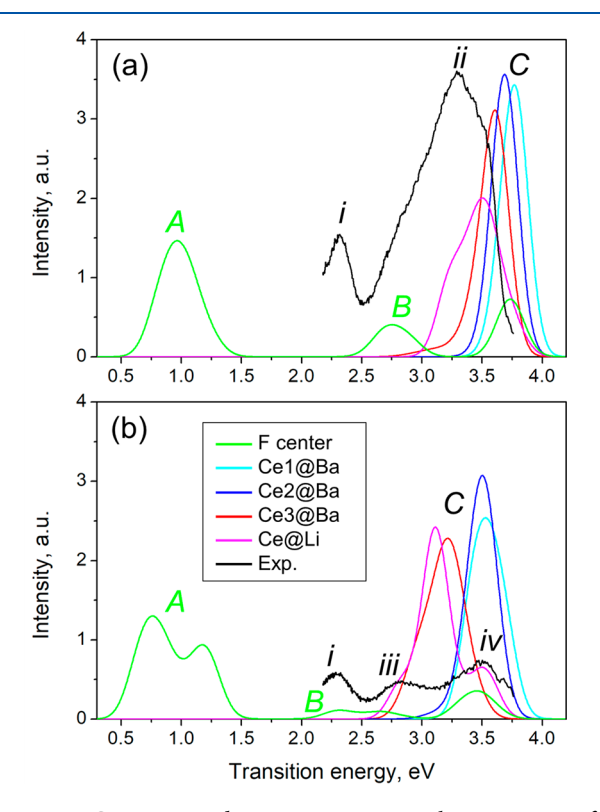


Figure 8. Comparison between experimental PL spectra for LBBF:Ce³⁺ crystals and computed MDPL spectra for the F-center, Ce1@Ba, Ce2@Ba, Ce3@Ba, and Ce@Li models. Molecular dynamics calculations are carried out using SP DFT for the F-center and NCS DFT for the other models. For MDPL spectra of the F-center, one combines the contributions from spin up and spin down components. Spectra from panel a are obtained at 77 K, while spectra in panel b are obtained at 300 K.

between experimental PL spectra for LBBF:Ce³+ crystals and computed MDPL spectra for F-center, Ce1@Ba, Ce2@Ba, Ce3@Ba, and Ce@Li models. Note that the MDPL spectra are computed using PBE functional, thus showing smaller transition energies than time-integrated PL spectra in Figure 7 based on HSE06 functional. MD calculations are carried out using SP DFT for the F-center and NCS DFT for the other models. MDPL spectra of the spin up component of F-center include three transitions i.e. HO-1 \rightarrow HO, LU \rightarrow HO-1, and LU \rightarrow HO, whereas MDPL spectra of other models only include LU \rightarrow HO transitions, as suggested by the time-integrated PL spectra along excited-state trajectories. For MDPL spectra of the F-center, one combines the contributions from spin up and spin down components.

The top (a) and bottom (b) panels of Figure 8 show PL at 77 and 300 K, respectively. The experimental PL spectra display two emission bands: the one with maximum at \sim 2.3 eV (feature i) and the other ranging from \sim 2.5 to 3.7 eV (features ii, iii, and iv). The interpretation of experimental data attributes band i to intrinsic defects and bands ii-iv to the Ce³⁺ emission. The MDPL spectra display three distinct features, namely the interband transition "A" and intraband transition "B" from the F-center model, and transition "C" mainly contributed by Ce³⁺ containing models. Here we propose two hypothetic explanations for the similarities and differences

between experimental and computed PL spectra. The first hypothetic explanation is that features i and ii—iv correspond to features "B" and "C", respectively. The range of energies below ~2.3 eV is not studied experimentally. Therefore, the feature "A" is predicted to be possible by theory but is not observed on experiment. At 77 K, there is an offset of about 0.4 eV between MDPL and experimental PL spectra. MDPL spectra at 300 K show redshifts of emission and line-width broadening compared to the ones at 77 K and agree better with experimental PL in terms of transition energies. Feature iii can be mainly attributed to transitions of Ce@Li and Ce3@Ba, while feature iv to transitions of Ce1@Ba and Ce2@Ba. The second hypothetical explanation is that feature i corresponds to feature " \hat{A} ". Feature \hat{i} is not resolved and can be attributed to features "B" and "C" at 77 K. Features iii and iv correspond to features "B" and "C" at 300 K, respectively. In this case, the transition energy difference between features "A" and "B" is about 1.7 eV, which is much larger than the corresponding experimental values ($\sim 1.0 \text{ eV}$ between features *i* and *ii* or ~ 0.5 eV between features i and iii). However, one should bear in mind that this transition energy difference depends on the energy level of trap states, which is expected to change by adopting different exchange-correlation DFT functionals. Further experiments are needed to determine which of these hypothetical explanations is correct. Nonetheless, these explanations both suggest the broad emission band of experimental PL is mainly due to emission of Ce³⁺, whereas the presence of F-center contributes to the low intensity features at higher wavelengths.

4. CONCLUSIONS

In summary, we perform DFT calculations to obtain ground state electronic structures of various Ce-containing LBBF models where doping atoms are located at different sites of the host lattice. It is found that the optical properties of Ce-doped borates are determined by 5d-4f transitions on Ce³⁺ ions. We also consider the presence of the F-center, which exhibits a trap state with energy within the band gap. NACs are calculated in the basis of adiabatic MD trajectories to obtain nonradiative relaxation rates of electrons and holes. Timeintegrated PL spectra based on NACs and MDPL spectra are generated, the latter oneshows a qualitative agreement with experimental PL spectra by accounting for the effect of thermal broadening. One finds that relaxation rates, transition energies, and intensities of Ce-containing LBBF models depend on the spatial location of doping sites. Our study shows that the broad emission bands of experimental PL of Ce³⁺ doped LBBF have two components. The one at the lower transition energy is attributed to transitions from trap state of F-center, whereas the other one at the higher transition energy is mainly due to Kasha emission from Ce3+ species. This combined experimental and computational effort contributes to the identification and interpretation of probable and promising synthetic pathways to create efficient light emitters.

ASSOCIATED CONTENT

Supporting Information

The Supporting Information is available free of charge at https://pubs.acs.org/doi/10.1021/acs.jpcc.2c08711.

Total energies of Ce@Ba structures, autocorrelation functions of nonadiabatic couplings, Redfield tensors representing hot carrier cooling, and dynamics of

excitation energy dissipation for F-center spin α , F-center spin β , Ce2@Ba, and Ce@Li models at 77 and 300 K. (PDF)

AUTHOR INFORMATION

Corresponding Authors

Tatyana B. Bekker — Sobolev Institute of Geology and Mineralogy, Siberian Branch of Russian Academy of Science, 630090 Novosibirsk, Russia; Novosibirsk State University of Architecture, Design and Arts (NSUADA), 630099 Novosibirsk, Russia; Novosibirsk State University, 630090 Novosibirsk, Russia; Email: bekker@igm.nsc.ru

Dmitri S. Kilin — North Dakota State University, Fargo, North Dakota 58108, United States; oorcid.org/0000-0001-7847-5549; Email: dmitri.kilin@ndsu.edu

Authors

Talgat M. Inerbaev — Sobolev Institute of Geology and Mineralogy, Siberian Branch of Russian Academy of Science, 630090 Novosibirsk, Russia; L. N. Gumilyov Eurasian National University, Astana 010008, Kazakhstan; Novosibirsk State University, 630090 Novosibirsk, Russia; orcid.org/0000-0003-2378-4082

Yulun Han – North Dakota State University, Fargo, North Dakota 58108, United States

Complete contact information is available at: https://pubs.acs.org/10.1021/acs.jpcc.2c08711

Notes

The authors declare no competing financial interest.

ACKNOWLEDGMENTS

This work was supported by the Russian Science Foundation, Grant No. 21-19-00097, www.rscf.ru/project/21-19-00097/. D.S.K. and Y.H. acknowledge partial support from the U.S. Department of Energy DE-SC0022239 for computational exploration of photoluminescence of metal centers. D.S.K., Y.H., and T.M.I. acknowledge the resources of the DOE BES NERSC facility. We are grateful to the Supercomputer Center, Novosibirsk State University, for access to the resources of the cluster.

REFERENCES

- (1) Chen, C.; Sasaki, T.; Li, R.; Wu, Y.; Lin, Z.; Mori, Y.; Hu, Z.; Wang, J.; Aka, G.; Yoshimura, M. Nonlinear Optical Borate Crystals: Principals and Applications; John Wiley & Sons: 2012.
- (2) Mutailipu, M.; Poeppelmeier, K. R.; Pan, S. Borates: A Rich Source for Optical Materials. *Chem. Rev.* **2021**, *121*, 1130–1202.
- (3) Tawalare, P. K. Luminescent Inorganic Mixed Borate Phosphors Materials for Lighting. *Luminescence* **2022**, *37*, 1226–1245.
- (4) Chopra, V.; Kadam, A. R.; Swart, H. C.; Dhoble, S. J., Chapter 1 Introduction to Luminescence and Radiation Dosimetry Techniques. In *Radiation Dosimetry Phosphors*; Dhoble, S., Chopra, V., Nayar, V., Kitis, G., Poelman, D., Swart, H., Eds.; Woodhead Publishing: 2022; pp 1–27.
- (5) Omar, R. S.; Dhoble, S. J., Chapter 14 Dosimetric Properties of Gamma-Irradiated Borate Materials. In *Radiation Dosimetry Phosphors*, Dhoble, S., Chopra, V., Nayar, V., Kitis, G., Poelman, D., Swart, H., Eds.; Woodhead Publishing: 2022; pp 355–403.
- (6) Taki, T.; Strassburg, M. Review—Visible Leds: More Than Efficient Light. ECS J. Solid State Sci. Technol. 2020, 9, 015017.
- (7) Zhang, J.; Wang, M.; Fang, Z.; Lai, X.; Zhong, Z.; Zhang, R. A Novel White-Light-Emitting Phosphor Based on Bi3+-Doped

- Balu2mgga2si2o12 for near-Uv Excited White Leds. ECS J. Solid State Sci. Technol. 2021, 10, 055011.
- (8) Bertram, D.; Born, M.; Jüstel, T., Incoherent Light Sources. In *Springer Handbook of Lasers and Optics*; Träger, F., Ed.; Springer New York: New York, 2007; pp 565–582.
- (9) Cho, J.; Park, J. H.; Kim, J. K.; Schubert, E. F. White Light-Emitting Diodes: History, Progress, and Future. *Laser Photonics Rev.* **2017**, *11*, 1600147.
- (10) Revankar, S. G.; Gedekar, K. A.; Moharil, S. V. Luminescent Materials Based on Aluminates: A Review. *Phys. Status Solidi A* **2022**, 219, 2200346.
- (11) Fernández-Rodríguez, L.; Durán, A.; Pascual, M. J. Silicate-Based Persistent Phosphors. *Open Ceram.* **2021**, *7*, 100150.
- (12) Lin, Y.-C.; Karlsson, M.; Bettinelli, M. Inorganic Phosphor Materials for Lighting. *Top. Curr. Chem.* **2016**, *374*, 21.
- (13) Phillips, J. M.; et al. Research Challenges to Ultra-Efficient Inorganic Solid-State Lighting. *Laser Photonics Rev.* **2007**, *1*, 307–333.
- (14) Bachmann, V.; Ronda, C.; Meijerink, A. Temperature Quenching of Yellow Ce3+ Luminescence in Yag:Ce. *Chem. Mater.* **2009**, 21, 2077–2084.
- (15) Jang, H. S.; Won, Y. H.; Jeon, D. Y. Improvement of Electroluminescent Property of Blue Led Coated with Highly Luminescent Yellow-Emitting Phosphors. *Appl. Phys. B: Laser Opt.* **2009**, *95*, 715–720.
- (16) Huang, X. Red Phosphor Converts White Leds. Nat. Photonics 2014, 8, 748–749.
- (17) Ahn, Y. N.; Kim, K. D.; Anoop, G.; Kim, G. S.; Yoo, J. S. Design of Highly Efficient Phosphor-Converted White Light-Emitting Diodes with Color Rendering Indices $(R1-R15) \ge 95$ for Artificial Lighting. *Sci. Rep.* **2019**, *9*, 16848.
- (18) Liu, Y.; Zhang, X.; Hao, Z.; Lu, W.; Liu, X.; Wang, X.; Zhang, J. Crystal Structure and Luminescence Properties of (Ca2.94–Xluxce0.06)(Sc2–Ymgy)Si3o12 Phosphors for White Leds with Excellent Colour Rendering and High Luminous Efficiency. *J. Phys. D: Appl. Phys.* **2011**, *44*, 075402.
- (19) Li, J.; Li, J.-G.; Liu, S.; Li, X.; Sun, X.; Sakka, Y. Greatly Enhanced Dy3+ Emission Via Efficient Energy Transfer in Gadolinium Aluminate Garnet (Gd3al5o12) Stabilized with Lu3+. J. Mater. Chem. C 2013, 1, 7614–7622.
- (20) Ding, J.; Kuang, M.; Liu, S.; Zhang, Z.; Huang, K.; Huo, J.; Ni, H.; Zhang, Q.; Li, J. Sensitization of Mn2+ Luminescence Via Efficient Energy Transfer to Suit the Application of High Color Rendering Wleds. *Dalton Trans.* **2022**, *51*, 9501–9510.
- (21) Geng, W.; Zhou, X.; Ding, J.; Wang, Y. Density-Functional Theory Calculations, Luminescence Properties and Fluorescence Ratiometric Thermo-Sensitivity for a Novel Borate Based Red Phosphor: Nabasc(Bo3)2:Ce3+,Mn2+. *J. Mater. Chem. C* **2019**, 7, 1982–1990.
- (22) Zhang, D.; Li, G.; Leng, Z.; Li, L. Site Occupancy and Tunable Photoluminescence Properties of Eu2+-Activated Ba3sc(Bo3)3 Phosphors for White Light Emitting Diodes. *J. Alloys Compd.* **2020**, *815*, 152645.
- (23) Wang, S.; Xu, Y.; Chen, T.; Jiang, W.; Liu, J.; Zhang, X.; Jiang, W.; Wang, L. A Red Phosphor Lasc3(Bo3)4:Eu3+ with Zero-Thermal-Quenching and High Quantum Efficiency for Leds. *Chem. Eng. J.* 2021, 404, 125912.
- (24) Ding, X.; Wang, Y. Commendable Eu2+-Doped Oxide-Matrix-Based Liba12(Bo3)7f4 Red Broad Emission Phosphor Excited by Nuv Light: Electronic and Crystal Structures, Luminescence Properties. ACS Appl. Mater. Interfaces 2017, 9, 23983–23994.
- (25) Li, B.; Huang, X.; Lin, J. Single-Phased White-Emitting Ca3y(Gao)3(Bo3)4:Ce3+,Tb3+,Sm3+ Phosphors with High-Efficiency: Photoluminescence, Energy Transfer and Application in near-Uv-Pumped White Leds. J. Lumin. 2018, 204, 410–418.
- (26) Li, B.; Sun, Q.; Wang, S.; Guo, H.; Huang, X. Ce3+ and Tb3+ Doped Ca3gd(Alo)3(Bo3)4 Phosphors: Synthesis, Tunable Photoluminescence, Thermal Stability, and Potential Application in White Leds. *RSC Adv.* **2018**, *8*, 9879–9886.

- (27) Zhao, J.; Li, R. K. Two New Barium Borate Fluorides Aba12(Bo3)7f4 (a = Li and Na). *Inorg. Chem.* **2014**, 53, 2501–2505.
- (28) Bekker, T. B.; Rashchenko, S. V.; Solntsev, V. P.; Yelisseyev, A. P.; Kragzhda, A. A.; Bakakin, V. V.; Seryotkin, Y. V.; Kokh, A. E.; Kokh, K. A.; Kuznetsov, A. B. Growth and Optical Properties of Lixna1—Xba12(Bo3)7f4 Fluoride Borates with "Antizeolite" Structure. *Inorg. Chem.* **2017**, *56*, 5411—5419.
- (29) Bekker, T. B.; Inerbaev, T. M.; Yelisseyev, A. P.; Solntsev, V. P.; Rashchenko, S. V.; Davydov, A. V.; Shatskiy, A. F.; Litasov, K. D. Experimental and Ab Initio Studies of Intrinsic Defects in "Antizeolite" Borates with a Ba12(Bo3)66+ Framework and Their Influence on Properties. *Inorg. Chem.* 2020, 59, 13598–13606.
- (30) Bekker, T. B.; Ryadun, A. A.; Davydov, A. V.; Solntsev, V. P.; Grigorieva, V. D. Luminescence Properties of Rare-Earth-Doped Fluoride Borate Crystals. *J. Alloys Compd.* **2022**, *900*, 163343.
- (31) Inerbaev, T. M.; Han, Y.; Bekker, T. B.; Kilin, D. S. Mechanisms of Photoluminescence in Copper-Containing Fluoride Borate Crystals. *J. Phys. Chem. C* **2022**, *126*, 6119–6128.
- (32) Yao, G.; Berry, M. T.; May, P. S.; Kilin, D. Dft Calculation of Russell—Saunders Splitting for Lanthanide Ions Doped in Hexagonal (B)-Nayf4 Nanocrystals. *J. Phys. Chem. C* **2013**, *117*, 17177—17185.
- (33) Yao, G.; Huang, S.; Berry, M. T.; May, P. S.; Kilin, D. S. Non-Collinear Spin Dft for Lanthanide Ions in Doped Hexagonal Nayf4. *Mol. Phys.* **2014**, *112*, 546–556.
- (34) Vogel, D. J.; Kilin, D. S. First-Principles Treatment of Photoluminescence in Semiconductors. *J. Phys. Chem. C* **2015**, *119*, 27954–27964.
- (35) Yao, G.; Meng, Q.; Berry, M. T.; May, P. S.; S. Kilin, D. Molecular Dynamics in Finding Nonadiabatic Coupling for B-Nayf4: Ce3+ Nanocrystals. *Mol. Phys.* **2015**, *113*, 385–391.
- (36) Han, Y.; Vogel, D. J.; Inerbaev, T. M.; May, P. S.; Berry, M. T.; Kilin, D. S. Photoinduced Dynamics to Photoluminescence in Ln3+ (Ln = Ce, Pr) Doped B-Nayf4 Nanocrystals Computed in Basis of Non-Collinear Spin Dft with Spin-Orbit Coupling. *Mol. Phys.* **2018**, *116*, 697–707.
- (37) Kharabe, V. R.; Dhoble, S. J.; Moharil, S. V. Synthesis of Dy3+ and Ce3+ Activated Sr6bp5o20 and Ca6bp5o20 Borophosphate Phosphors. *J. Phys. D: Appl. Phys.* **2008**, *41*, 205413.
- (38) Shinde, K. N.; Dhoble, S. J. 5d-4f Transition in New Phosphate-Based Phosphors. *Luminescence* **2012**, 27, 69-73.
- (39) Hou, D.; Han, B.; Chen, W.; Liang, H.; Su, Q.; Dorenbos, P.; Huang, Y.; Gao, Z.; Tao, Y. Luminescence of Ce3+ at Two Different Sites in A-Sr2p2o7 under Vacuum Ultraviolet-Uv and X-Ray Excitation. *J. Appl. Phys.* **2010**, *108*, 083527.
- (40) Putaj, P.; de Haas, J. T. M.; Kramer, K. W.; Dorenbos, P. Optical and Scintillation Properties of the Thermal Neutron Scintillator Li\$_{3}\$ Ycl\$_{6}\$:Ce. *IEEE Trans. Nucl. Sci.* **2010**, 57, 1675–1681.
- (41) Feng, H.; Ding, D.; Li, H.; Lu, S.; Pan, S.; Chen, X.; Ren, G. Cerium Concentration and Temperature Dependence of the Luminescence of Lu2si2o7:Ce Scintillator. *J. Alloys Compd.* **2011**, 509, 3855–3858.
- (42) Shendrik, R. Y.; Kovalev, I. I.; Rusakov, A. I.; Sokol'nikova, Y. V.; Shalaev, A. A. Luminescence of Babri Crystals Doped with Ce3+Ions. *Phys. Solid State* **2019**, *61*, 830–834.
- (43) Bünzli, J.-C. G.; Comby, S.; Chauvin, A.-S.; Vandevyver, C. D. B. New Opportunities for Lanthanide Luminescence. *J. Rare Earths* **2007**, 25, 257–274.
- (44) Blasse, G. In The Influence of Charge-Transfer and Rydberg States on the Luminescence Properties of Lanthanides and Actinides, Spectra and Chemical Interactions; Braterman, P. S., Blasse, G., Müller, A., Baran, E. J., Carter, R. O., Eds.; Springer Berlin Heidelberg: Berlin and Heidelberg, Germany, 1976; pp 43–79.
- (45) Dorenbos, P. The 4fn → 4fn − 15d Transitions of the Trivalent Lanthanides in Halogenides and Chalcogenides. *J. Lumin.* **2000**, *91*, 91–106
- (46) Xia, Z.; Meijerink, A. Ce3+-Doped Garnet Phosphors: Composition Modification, Luminescence Properties and Applications. *Chem. Soc. Rev.* **2017**, *46*, 275–299.

- (47) Goyal, P.; Schwerdtfeger, C. A.; Soudackov, A. V.; Hammes-Schiffer, S. Nonadiabatic Dynamics of Photoinduced Proton-Coupled Electron Transfer in a Solvated Phenol–Amine Complex. *J. Phys. Chem. B* **2015**, *119*, 2758–2768.
- (48) Redfield, A. G. On the Theory of Relaxation Processes. *IBM J. Res. Dev.* **1957**, *1*, 19–31.
- (49) Micha, D. A.; Leathers, A. S. Reduced Density Matrix Equations for Combined Instantaneous and Delayed Dissipation in Many-Atom Systems, and Their Numerical Treatment. In *Energy Transfer Dynamics in Biomaterial Systems*; Burghardt, I., May, V., Micha, D. A., Bittner, E. R., Eds. Springer Berlin Heidelberg: Berlin and Heidelberg, Germany, 2009; pp 363–380.
- (50) Kilin, D. S.; Micha, D. A. Relaxation of Photoexcited Electrons at a Nanostructured Si(111) Surface. *J. Phys. Chem. Lett.* **2010**, *1*, 1073–1077.
- (51) Inerbaev, T.; Forde, A.; Jensen, S. J.; Kilin, D., Spin-Unrestricted and Spinor Nonradiative Relaxation Dynamics in Functionalized Semiconductors. In *Computational Photocatalysis: Modeling of Photophysics and Photochemistry at Interfaces*; American Chemical Society: 2019; Vol. 1331, pp 1–22.
- (52) Vazhappilly, T.; Han, Y.; Kilin, D. S.; Micha, D. A. Electronic Relaxation of Photoexcited Open and Closed Shell Adsorbates on Semiconductors: Ag and Ag2 on Tio2. *J. Chem. Phys.* **2022**, *156*, 104705.
- (53) Chen, J.; Schmitz, A.; Inerbaev, T.; Meng, Q.; Kilina, S.; Tretiak, S.; Kilin, D. S. First-Principles Study of P-N-Doped Silicon Quantum Dots: Charge Transfer, Energy Dissipation, and Time-Resolved Emission. *J. Phys. Chem. Lett.* **2013**, *4*, 2906–2913.
- (54) Steiner, S.; Khmelevskyi, S.; Marsmann, M.; Kresse, G. Calculation of the Magnetic Anisotropy with Projected-Augmented-Wave Methodology and the Case Study of Disordered Fe_{1-x}Co_x Alloys. *Phys. Rev. B* **2016**, 93, 224425.
- (55) Vogel, D. J.; Inerbaev, T. M.; Kilin, D. S. Role of Lead Vacancies for Optoelectronic Properties of Lead-Halide Perovskites. *J. Phys. Chem. C* **2018**, *122*, 5216–5226.
- (56) Vogel, D. J.; Kryjevski, A.; Inerbaev, T.; Kilin, D. S. Photoinduced Single- and Multiple-Electron Dynamics Processes Enhanced by Quantum Confinement in Lead Halide Perovskite Quantum Dots. J. Phys. Chem. Lett. 2017, 8, 3032–3039.
- (57) Han, Y.; Meng, Q.; Rasulev, B.; May, P. S.; Berry, M. T.; Kilin, D. S. Photoinduced Charge Transfer Versus Fragmentation Pathways in Lanthanum Cyclopentadienyl Complexes. *J. Chem. Theory Comput.* **2017**, *13*, 4281–4296.
- (58) Kresse, G.; Joubert, D. From Ultrasoft Pseudopotentials to the Projector Augmented-Wave Method. *Phys. Rev. B* **1999**, *59*, 1758–1775.
- (59) Kresse, G.; Furthmüller, J. Efficient Iterative Schemes for Ab Initio Total-Energy Calculations Using a Plane-Wave Basis Set. *Phys. Rev. B* **1996**, *54*, 11169–11186.
- (60) Perdew, J. P.; Burke, K.; Ernzerhof, M. Generalized Gradient Approximation Made Simple. *Phys. Rev. Lett.* **1996**, *77*, 3865–3868.
- (61) Perdew, J. P.; Chevary, J. A.; Vosko, S. H.; Jackson, K. A.; Pederson, M. R.; Singh, D. J.; Fiolhais, C. Atoms, Molecules, Solids, and Surfaces: Applications of the Generalized Gradient Approximation for Exchange and Correlation. *Phys. Rev. B* **1992**, *46*, 6671–6687.
- (62) Heyd, J.; Scuseria, G. E.; Ernzerhof, M. Hybrid Functionals Based on a Screened Coulomb Potential. *J. Chem. Phys.* **2003**, *118*, 8207–8215.
- (63) Bekker, T. B.; Yelisseyev, A. P.; Solntsev, V. P.; Davydov, A. V.; Inerbaev, T. M.; Rashchenko, S. V.; Kostyukov, A. I. The Influence of Co-Doping on the Luminescence and Thermoluminescence Properties of Cu-Containing Fluoride Borate Crystals. *CrystEngComm* **2021**, 23, 6599–6609.
- (64) Dudarev, S. L.; Botton, G. A.; Savrasov, S. Y.; Humphreys, C. J.; Sutton, A. P. Electron-Energy-Loss Spectra and the Structural Stability of Nickel Oxide: An Lsda+U Study. *Phys. Rev. B* **1998**, *57*, 1505–1509.

- (65) Inerbaev, T. M.; Seal, S.; Masunov, A. E. Density Functional Study of Oxygen Vacancy Formation and Spin Density Distribution in Octahedral Ceria Nanoparticles. *J. Mol. Model.* **2010**, *16*, 1617–1623.
- (66) Blöchl, P. E. Projector Augmented-Wave Method. Phys. Rev. B 1994, 50, 17953-17979.
- (67) Verlet, L. Computer "Experiments" on Classical Fluids. I. Thermodynamical Properties of Lennard-Jones Molecules. *Phys. Rev.* **1967**, *159*, 98–103.
- (68) Momma, K.; Izumi, F. Vesta: A Three-Dimensional Visualization System for Electronic and Structural Analysis. *J. Appl. Crystallogr.* **2008**, *41*, 653–658.
- (69) Wang, V.; Xu, N.; Liu, J.-C.; Tang, G.; Geng, W.-T. Vaspkit: A User-Friendly Interface Facilitating High-Throughput Computing and Analysis Using Vasp Code. Comput. Phys. Commun. 2021, 267, 108033.
- (70) Han, Y.; Anderson, K.; Hobbie, E. K.; Boudjouk, P.; Kilin, D. S. Unraveling Photodimerization of Cyclohexasilane from Molecular Dynamics Studies. *J. Phys. Chem. Lett.* **2018**, *9*, 4349–4354.

☐ Recommended by ACS

Investigation of Structural, Mechanical, Optoelectronic, and Thermoelectric Properties of $BaXF_3$ (X = Co, Ir) Fluoro-Perovskites: Promising Materials for Optoelectronic and...

Shaukat Ali Khattak, Vineet Tirth, et al.

FEBRUARY 01, 2023 ACS OMEGA

READ 🗹

Real-Space Infrared Spectroscopy of Ferroelectric Domain Walls in Multiferroic h-(Lu,Sc)FeO₃

Kevin A. Smith, Janice L. Musfeldt, et al.

JANUARY 30, 2023

ACS APPLIED MATERIALS & INTERFACES

READ 🗹

Ion Irradiation Effects on Two-Dimensional MXene Ti₂C for Applications in Extreme Conditions: Combined Ab Initio and Monte Carlo Simulations

Tianzhao Li, Miao Zhou, et al

FEBRUARY 22, 2023

ACS APPLIED NANO MATERIALS

READ 🗹

Structural Defect Effect on the Concentration Quenching of $Tb_xY_{2-x}O_3$ Phosphor Thin Films

Shizuka Suzuki, Ryota Takahashi, et al.

MAY 09, 2023

THE JOURNAL OF PHYSICAL CHEMISTRY C

READ 🗹

Get More Suggestions >